The temperature-dependent microstructure of PEDOT/PSS films: insights from morphological, mechanical and electrical analyses

Item Type	Article
Authors	Zhou, Jian; Anjum, Dalaver H.; Chen, Long; Xu, Xuezhu; Ventura, Isaac Aguilar; Jiang, Long; Lubineau, Gilles
Citation	The temperature-dependent microstructure of PEDOT/PSS films: insights from morphological, mechanical and electrical analyses 2014, 2 (46):9903 J. Mater. Chem. C
Eprint version	Post-print
DOI	10.1039/C4TC01593B
Publisher	Royal Society of Chemistry (RSC)
Journal	J. Mater. Chem. C
Rights	Archived with thanks to J. Mater. Chem. C
Download date	10/08/2022 04:31:20
Link to Item	http://hdl.handle.net/10754/558857

PAPER

The temperature-dependent microstructure of PEDOT/PSS films: insights from morphological, mechanical and electrical analyses†

Jian Zhou,[*a] Dalaver H. Anjum,[b] Long Chen,[b] Xuezhu Xu,[c] Isaac Aguilar Ventura,[a] Long Jiang[c] and Gilles Lubineau[*a]

Poly(3,4-ethylenedioxythiophene)/poly(styrenesulfonate) (PEDOT/PSS) is a widely used conductive polymer in the field of flexible electronics. The ways its microstructure changes over a broad range of temperatures remain unclear. This paper describes microstructure changes at different temperatures and correlates the microstructure with its physical properties (mechanical and electrical). We used High-Angle Annular Dark-Field Scanning Electron Microscopy (HAADF-STEM) combined with electron energy loss spectroscopy (EELS) to determine the morphology and elemental atomic ratio of the film at different temperatures. These results together with the Atomic Force Microscopy (AFM) analysis provide the foundation for a model of how the temperature affects the microstructure of PEDOT/PSS. Moreover, dynamic mechanical analysis (DMA) and electrical characterization were performed to analyze the microstructure and physical property correlations.

1 Introduction

Conductive polymers have easily tailorable electrical, mechanical and optical properties that make them good candidate materials for applications such as touch panels, light-emitting diodes, thermoelectric devices, solar cells, sensors and actuators.[1–10] Poly(3,4-ethylenedioxythiophene)/poly(styrenesulfonate) (PEDOT/PSS) is one of the most successful polymers in the family of conductive polymers.[2,11] Great efforts have been devoted to understanding and improving the electrical conductivity of PEDOT/PSS, which was demonstrated to be tailorable in a wide range between 0.1 and 4380 S cm^{-1} by using solvent treatments.[12–18]

A main feature of this material is that its mechanical, thermo-mechanical and piezo behaviors are highly dependent on its water content.[19] The Young's modulus of PEDOT/PSS thin films dramatically reduces when the relative humidity (RH) of the surrounding environment increases. This was attributed to the water uptake by the hygroscopic PSS phase that weakens the cohesion between PEDOT/PSS grains.[19,20] Recently the behavior

of our PEDOT/PSS-based paper actuators was also shown to display high dependency on RH levels.[21–24] The mechanism behind PEDOT/PSS-based actuators lies in controlled water absorption/desorption. Such actuators are controlled by an input electrical current which uses the Joule effect to generate a change in the temperature of the sample. This change in temperature in turn induces water absorption or desorption and a mechanical response of the actuator. These results suggest that water absorbed on PEDOT/PSS plays an important role in determining the final mechanical behaviors of the PEDOT/PSS films. Indeed, dimensional and physical (mechanical and electrical) stabilities of conductive polymers are important to their use in organic devices where they may encounter a wide variation in temperature through their operating lifetimes/conditions. High-resolution microstructure characterization is needed to study this complex material and can help us to obtain critical information about the origin of its physical properties. Until now, only a few microscopical studies on PEDOT/PSS films have been carried out. Research has revealed the core–shell structure of PEDOT/PSS grains by High-Angle Annular Dark-Field Scanning Electron Microscopy (HAADF-STEM) at room temperature.[25] However, the change in the microstructure over a broad range of temperatures has not been studied. The objective of this work is to monitor these microstructural changes at different temperatures and correlate them with the observed changes in the macroscopic physical behavior of PEDOT/PSS films.

In detail, we used HAADF-STEM combined with electron energy loss spectroscopy (EELS) to determine the morphology and elemental atomic ratio of the PEDOT/PSS film at different

[a]King Abdullah University of Science and Technology (KAUST), Physical Sciences and Engineering Division, COHMAS Laboratory, Thuwal 23955-6900, Saudi Arabia. E-mail: zhouj588@gmail.com; gilles.lubineau@kaust.edu.sa; Tel: +966(12)8082983
[b]King Abdullah University of Science and Technology (KAUST), Advanced Nanofabrication, Imaging and Characterization Core Laboratory, Thuwal 23955-6900, Saudi Arabia
[c]North Dakota State University, Department of Mechanical Engineering, Fargo, ND 58108, USA
† Electronic supplementary information (ESI) available. See DOI: 10.1039/c4tc01593b

temperatures. These observations, completed by Atomic Force Microscopy (AFM) analysis, provide us with a basis to propose a microscopic model at different temperatures. To give a better understanding of the model, we investigated the thermal properties of PEDOT/PSS by using Differential scanning calorimetry (DSC) and Thermogravimetric Analysis (TGA). In order to correlate the microstructural changes with the physical properties of PEDOT/PSS, we then examined the dynamic mechanical behavior and electrical conductivity of PEDOT/PSS films, in the temperature range of −150 to 250 °C. Such correlations will be important tools for understanding the physical properties of PEDOT/PSS and for evaluating its potential in electronic devices.

2 Experimental

2.1 Materials

An aqueous dispersion of PEDOT/PSS, called Clevios™ P, was purchased from HC Starck, Inc. Acetone (ACS reagent, >99.5%) was purchased from Sigma-Aldrich. The AZ9210 photoresist was purchased from MicroChem. Silicon and quartz wafers were purchased from GlobalSpec.

2.2 Preparation of PEDOT/PSS films

PEDOT/PSS microfilms for DMA, DSC and TGA testing were prepared by casting 23 g of Clevios™ P aqueous solution on polycarbonate sheets with an area of 7×7 cm^2. The polycarbonate sheets were processed by hot pressing as described in previous studies.[24,26] The PEDOT/PSS films were dried in ambient air (21 °C, 65%RH) for 96 hours. Then, the film with a thickness of 50 ± 6 μm (measured by using a DM2020 digital micrometer, Digital Micrometers Ltd) was peeled off from the polycarbonate sheets and annealed in air at 120 °C for 4 hours.

PEDOT/PSS nanofilms for TEM imaging were prepared in a clean room to avoid contamination and the procedures are illustrated in Fig. S1:† (1) a silicon wafer was spincoated with a 10 μm AZ9210 photoresist film at a speed of 2400 rpm and baked at 110 °C for 180 s; (2) this photoresist was treated using an O$_2$ plasma cleaner to improve the hydrophilicity; (3) a dispersion of PEDOT/PSS was spincoated on the AZ9210-coated wafer at 5000 rpm and baked at 120 °C in air for 20 min; (4) samples were cut into small squares with dimensions of about 3 $\times$ 3 mm and immersed in an acetone bath, then 200 mesh holey-carbon copper grids (Pacific Grid Tech) were used to catch the PEDOT/PSS nanofilms that float off from the wafers. These samples were then air dried in ambient air (21 °C, RH at 65%) before observation.

We used quartz wafers to prepare uniform spin-coated PEDOT/PSS nanofilms for AFM imaging. These wafers with areas of 2.5×2.5 cm^2 were first placed for 1 min in an oxygen plasma cleaner for oxidation at 200 mtorr oxygen gas and 40 W of power. This process helped to remove the dust, improved the wettability of the glass substrate and finally enhanced the uniformity of the nanofilm. Spin-coating of PEDOT/PSS nanofilms was carried out on the treated quartz wafer at a speed of

5000 rpm for 60 s. These films were subsequently annealed on a hot plate at 120 °C for 20 min in an ambient atmosphere.

2.3 Characterization

TEM images of PEDOT/PSS were taken by using a Titan G^2 80-300 CT (FEI Company) at an accelerating voltage of 300 kV equipped with a field emission electron source. Combined with a low dose and high voltage imaging,[27] we were able to minimize the beam damage on the samples. The PEDOT/PSS samples were analyzed in Bright-Field TEM (BF-TEM) and High-Angle Annular Dark-Field Scanning Electron Microscopy (HAADF-STEM) observation modes. BF-TEM micrographs are digitally recorded by using an US4000 charged-couple device (CCD) camera (Gatan, Inc), while the HAADF-STEM micrographs are recorded with an analog detector (E. A. Fischione, Inc). In addition to this, electron energy loss spectroscopy (EELS) investigations, by setting the instrument in TEM-diffraction mode, were carried out using a GIF Tridiem™ post-column energy filter (Gatan, Inc). The specimens were loaded in the TEM chamber using a 621 cryo-transfer holder (Gatan, Inc). They were first investigated at room temperature (RT) and then cooled down to low temperature at −177 °C (LT) by filling the holder's Dewar flask with liquid nitrogen. Finally, the specimens were analyzed at high temperature (HT, 100 °C) which was controlled using a 900 Smartset temperature controller (Gatan, Inc). The samples used for imaging at LT and HT were stabilized for at least 1 hour. The entire image acquisition as well as processing of the data was performed using the GMS v1.8.3 microscopy suite software (Gatan, Inc).

Atomic Force Microscopy (AFM) images of spin-coated films on quartz wafers were taken using an Agilent 5400 (Agilent Technologies) microscope in the tapping mode over a window of 1 μm $\times$ 1 μm. Temperatures of the films were controlled either to RT or HT using a 325 temperature controller (Lake Shore Cryotronics, Inc.). Investigations at LT were not possible for AFM due to the technological limitations of our equipment. The films were maintained at each test temperature for at least 30 min before the AFM scanning. A rotated tip etched silicon probe (Bruker Corporation) with a high force constant (20–80 N m^{-1}) was used to improve the stability of the scanning at higher temperatures.

Differential Scanning Calorimetry (DSC) was carried out on PEDOT/PSS microfilms by using a TG 204 F1 instrument (NETZSCH Company). All operations were performed under nitrogen purge. The sample was first heated from 25 to 220 °C at 10 °C min^{-1}, followed by cooling down to 25 °C at 20 °C min^{-1}. Finally the sample was heated again from 25 to 220 °C at 10 °C min^{-1} to confirm whether or not the absorbed water molecules on PEDOT/PSS had been removed.

Thermogravimetric analysis (TGA) was performed on PEDOT/PSS microfilms by using a TG 209 F1 instrument (NETZSCH Company). All operations were performed under nitrogen purge. The sample was heated from 25 to 800 °C at a heating rate of 10 °C min^{-1}.

Dynamic Mechanical Analysis (DMA) was performed on rectangular samples (10 $\times$ 5 $\times$ 0.05 mm) on a DMA 242C

2 | J. Mater. Chem. C, 2014, xx, 1–8

This journal is © The Royal Society of Chemistry 2014

instrument (NETZSCH Company) in a tension mode. Initially, three scans of DMA measurements of the specimen were carried out in the temperature range of −150 to 220 °C, at 1 Hz frequency and a heating rate of 5 °C min⁻¹ (this heating rate was carefully chosen by considering our sample dimensions and testing mode),[28] and a cooling rate of 10 °C min⁻¹. Then, a multiple frequency scan (0.5, 1, 2, 5 and 10 Hz) was carried out to investigate the glass transition temperature of the film from −150 to 220 °C. During each heating and cooling process, a high purity N₂ purge was used (at a flow rate of 200 ml min⁻¹) to protect the sample and electronic devices used for measurement from high humidity in air.[29]

Electrical resistance, $R(T)$, of PEDOT/PSS films at different temperatures was measured using a U1252B multimeter (Agilent Technologies) by a two-point probe method. The sample with dimensions of $20 \times 8 \times 0.05$ mm was put into the DMA chamber to control the temperature and atmosphere. Silver epoxy was applied to the electrode on samples to ensure a good electrical connection to the multimeter. The distance between the two electrodes was 13 mm. The cooling and heating traces followed the aforementioned DMA temperature programs and are explained in the next section in detail. The electrical conductivity of PEDOT/PSS films at different temperatures was obtained by

$$\sigma(T) = \frac{L}{R(T)S} \tag{1}$$

where L is the distance between the electrodes (13 mm) and S is the cross-section area of the sample (0.05×8 mm).

3 Results and discussion

TEM and AFM imaging of PEDOT/PSS nanofilms

TEM imaging of PEDOT/PSS nanofilms was carried out at room (RT, 21 °C), low (LT, −177 °C) and high (HT, 100 °C) temperatures. Fig. S2† shows Energy-dispersive X-ray spectroscopy (EDX) spectra of the film on copper mesh and it reveals that the sample has a high purity. The traceable nitrogen (N), sodium (Na) and calcium (Ca) most likely stem from the catalyst during the fabrication process of Clevios P and this EDX result is in agreement with a former study.[25] Fig. 1(a) shows the BF-TEM image of the PEDOT/PSS nanofilm at RT. The granular structure of PEDOT/PSS could be observed with an average diameter of 30 ± 4 nm, though the contrast was very weak and the granular structure was somehow blurred. However, in the HAADF-STEM image of PEDOT/PSS at RT display enhanced contrast and individual grains could be clearly observed. The high magnification HAADF-STEM image confirmed the core–shell structures of PEDOT/PSS grains (Fig. 1(b)). The inset image of Fig. 1(b) shows the intensity distribution of the signal across one PEDOT/PSS grain at RT. The intensity at the border is higher than that at the center, which can help us to measure an average grain diameter of about 63 ± 12 nm and an average shell thickness of about 8 nm. Lang *et al.* also investigated the morphology of PEDOT/PSS nanofilms by TEM at room temperature and claimed that the individual grains have a PEDOT-rich core and a PSS-rich shell with a thickness of about
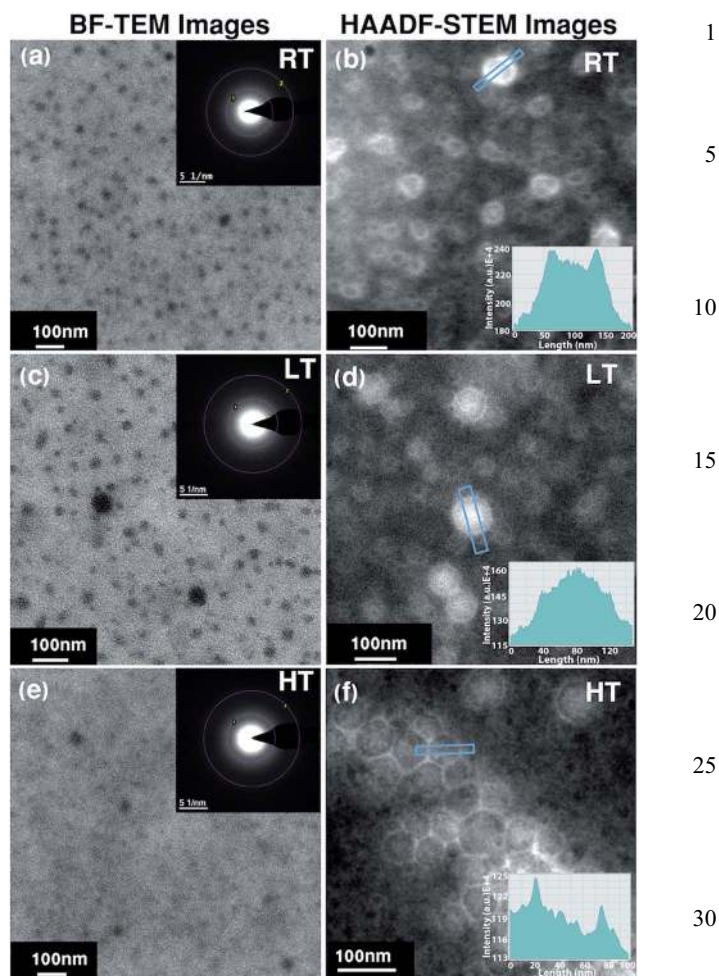

Fig. 1 Microstructure of PEDOT/PSS nanofilms. (a, c and e) BF-TEM images of PEDOT/PSS nanofilms at RT, LT and HT collected at a dose of 50 e⁻ Å⁻². Insets are TEM diffraction patterns. (b, d and f) HAADF-STEM images of PEDOT/PSS nanofilms at RT, LT and HT collected at a dose of 187 e⁻ Å⁻². Insets are corresponding profiles of PEDOT/PSS grains measured in the marked areas.

5–10 nm.[25] As we greatly increased the contrast in the HAADF-STEM image, there is a big difference in the diameter of the grains in the BF-TEM and HAADF-STEM images (Table S1, ESI†). Generally, the average diameter measured in the BF-TEM images was about 10–20 nm smaller than that measured in HADDF-STEM images (Table S1, ESI†). The reason behind this is that the PSS-rich shell or the ring area is invisible because of the low mass-thickness contrast developed from the sulfur–carbon areas in BF-TEM images.[27] In contrast, the *z*-contrast from the same region captured by HAADF-STEM becomes higher for the sulfur element. It is not the purpose of this paper to explain the difference between BF-TEM and HAADF-STEM techniques, but we do suggest that HAADF-STEM could be used as a better method to determine the morphology and diameter of PEDOT/PSS grains.

When it comes to LT, we found that the contrast of the BF-TEM image improved (Fig. 1(c)), which is due to the reduced thermal diffuse scattering of samples at low temperature and this effect greatly reduces the background intensity.[27] However,

This journal is © The Royal Society of Chemistry 2014

J. Mater. Chem. C, 2014, **xx**, 1–8 | **3**

Fig. 1(d) shows that the HAADF-STEM images at LT indicate no obvious core–shell structure of PEDOT/PSS grains. Even in PEDOT/PSS nanofilms sitting on carbon films, the bright rings surrounding the PEDOT-rich cores disappeared (Fig. S4, ESI†). The intensity distribution of the marked area in Fig. 1(d) indicates that the intensity at the border is lower than that at the center, which differs from the RT situation for which the core–shell structure was observed. These results indicate that the LT might induce a structure change in PEDOT/PSS grains, as the LT largely reduces the movement of the polymer chains. Also, when the specimen was cooled, it attracted water vapor, which condenses as ice on the surface of the sample.[27] To address this point further, background removed EELS spectra are used to quantify the elements of the film at the end of this section. Moreover, the hydrogen bonded water between the HSO_3 molecules was frozen, which restricted the movement of HSO_3 molecules and further reduced the movement of PSS polymer chains. As a result, in the core–shell structure at LT, the concentration of PSS in the shell was lower than at RT.

As far as the HT was concerned, we perceived that there was no water on the PEDOT/PSS film due to the heating. Fig. 1(e) shows that only a few of the PEDOT/PSS grains are observed, which is quite different from the BF-TEM images at RT and LT. Moreover, Fig. 1(f) shows that in the HAADF-TEM image, most of the PEDOT/PSS grains are connected to each other with bright boundaries. The average diameter of the grains is about 52 ± 10 nm. The intensity distribution of the marked area in Fig. 1(f) shows that the intensity in the connected area is higher than that in the non-connected area, indicating that the PEDOT/PSS grains overlap at the boundaries at HT. The morphology of the PEDOT/PSS film was also investigated at a higher temperature of 150 °C and is shown in Fig. S5, ESI†.† In both thin and thicker locations, most of the grains are connected to each other. These results indicate that after removing the hydrogen-bonded water molecules on the PEDOT/PSS film, the hydrogen-bonding interactions occur between HSO_3 groups on adjacent PSS chains (inter-molecular) or within different parts of single PSS chains (intra-molecular). Thus, the grains connect to adjacent neighbors. The hydrogen-bonds among HSO_3 participate in recovering part of the storage modulus at higher temperature after water removal. It is important to point out that the selected area electron diffraction (SAED) patterns of PEDOT/PSS nanofilms showed fuzzy-rings as can be seen in their corresponding electron micrographs in Fig. 1(a), (c) and (e). These characteristic rings do not show anisotropy in any direction. As expected, the PEDOT chains are randomly oriented in the spin-coated PEDOT/PSS films. Similar results have been reported for another conjugated polymer, polypyrrole, only isotropic rings were observed in as-deposited films.[30,31] Moreover, these SAEDs of PEDOT/PSS films showed no noticeable change in the *d*-spacings of crystal planes when measured at LT, RT and HT.

Fig. 2(a) shows background removed EELS spectra of the PEDOT/PSS nanofilms at three different temperatures. In the oxygen K-edge region from 532–560 eV, we observed intensity differences at different temperatures (Fig. 2(a)). Relative elemental quantification results of PEDOT/PSS nanofilms at
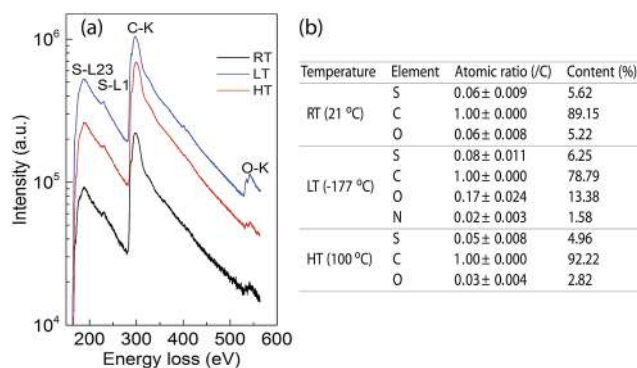

Fig. 2 (a) Electron energy loss spectroscopy of PEDOT/PSS nanofilms at RT, LT and HT. (b) Relative quantification of elements in PEDOT/PSS nanofilms from (a).

different temperatures are shown in Fig. 2(b). It reveals 89.15 at% carbon (C), 5.62 at% sulfur (S) and 5.22 at% oxygen (O) in PEDOT/PSS nanofilms at RT. These values are quite comparable with reported XPS values of PEDOT/PSS films that contain 85.7 at% C, 7.1 at% S and 6.7 at% O.[32] We can see from Fig. 2(b) that the percentage of S is relatively stable at different temperatures. However, the percentage of O increased from 5.22 (RT) to 13.38 at% (LT). The additional water comes from water vapor initially in the TEM chamber that condenses to have hydrogen bonding with HSO_3 segments in PSS chains. On the other hand, the O percentage reduced to 2.82 at% at HT, indicating that the free water/hydrogen-bonded water on PEDOT/PSS is largely removed. As a result, the oxygen probably only exists as sulfur-bonded O in PSS chains or as carbon-bonded O in PEDOT chains at HT.

Fig. 3 shows the AFM images of spincoated PEDOT/PSS nanofilms at RT and HT. The height and 3D images show that the PEDOT/PSS films are reasonably smooth on quartz wafers at different temperatures (Fig. 3(a), (c), (d) and (f)). It is difficult to identify single grains of PEDOT/PSS at RT due to the large amount of water absorbed on its surfaces. However, the grains were observed to be more aggregated at HT with an average diameter of 60 nm. The root mean square (rms) roughnesses estimated from the height images were 0.997 and 0.685 nm at
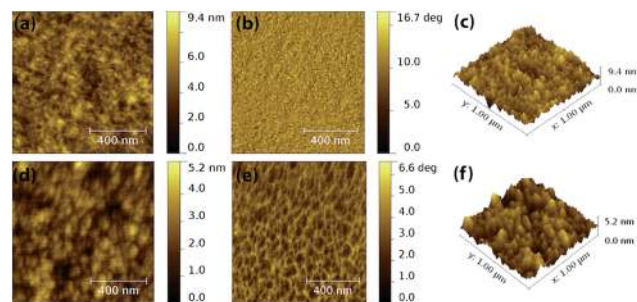

Fig. 3 AFM images of the spincoated PEDOT/PSS nanofilm at RT (a, b and c) and HT (d, e and f). (a) and (d) are height images, (b) and (e) are phase images, and (c) and (f) are 3D images. All the images are 1 μm × 1 μm.

4 | J. Mater. Chem. C, 2014, xx, 1–8

This journal is © The Royal Society of Chemistry 2014

RT and HT, respectively. The decrease in the rms roughness is induced by water removal at HT, as PEDOT/PSS grains fill the free space between PEDOT/PSS grains. Moreover, the phase image at HT shows that the grains are connected and over-lapped with adjacent neighbors at the borders (Fig. 3(e)). This result is in good agreement with HADDF-STEM images at HT (Fig. 1(h)), in which most of the PEDOT/PSS grains are con-nected to each other.

Structure insights and a microscopical model of the PEDOT/PSS film

By taking into account TEM and AFM image analyses at different temperatures, we can provide some insight into the evolution of the PEDOT/PSS microstructure with temperature. Generally, the PEDOT/PSS film contains core–shell structure grains having an average diameter of 40–60 nm. The core of the grain is a PEDOT nanocrystal,[33] together with a PSS-rich shell having an average thickness of 5–10 nm (Fig. 4). At room temperature and under a high humidity (65%), the hygroscopic PSS-rich shell readily takes up water vapor in air, as shown in Fig. 4.

In order to determine the role of the water in the micro-structure of PEDOT/PSS, thermal analysis was carried out on these films. Fig. 5(a) shows the DSC annealing and cooling traces of a PEDOT/PSS film. It is noted that due to the strong ionic bonding interaction between PEDOT and PSS, PEDOT/PSS does not have a well-defined glass transition value.[34] The PEDOT/PSS film exhibits a broad peak during the first anneal-ing while this peak disappeared during the second annealing. This indicates that the film released water during the heating process, as also observed by TGA (Fig. 5(b)). The first weight loss
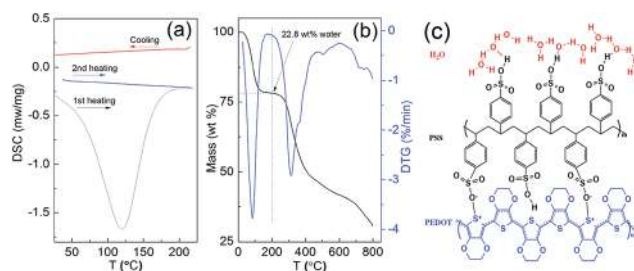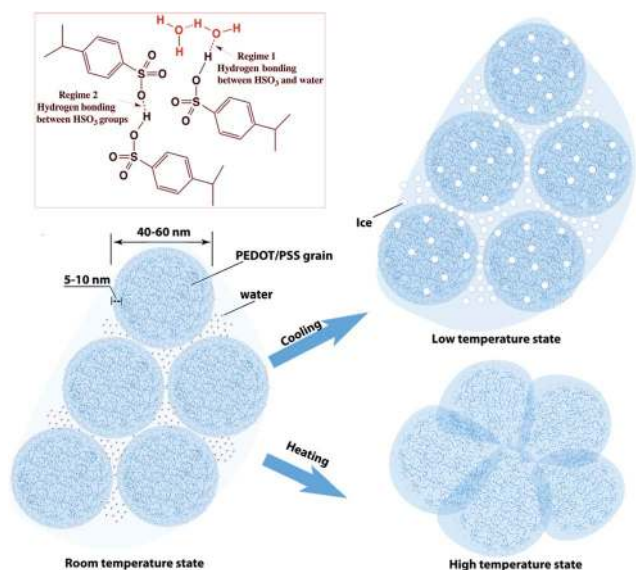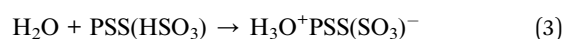

Fig. 4 Morphological models of PEDOT/PSS grains at different temperatures derived from combined TEM and AFM measurements. The typical diameter of PEDOT/PSS grains is 40–60 nm, with a PSS-rich shell thickness of 5–10 nm. The inset in the top-right corner depicts two regimes of hydrogen bonding in PEDOT/PSS.

Fig. 5 Thermal properties and molecular structure of the PEDOT/PSS film. (a) DSC thermograms of a PEDOT/PSS film, (b) TG and corre-sponding DTG curves of a PEDOT/PSS film, and (c) schematic of hydrogen bonding between PEDOT/PSS and water.

up to 120 °C can be ascribed to 20 wt% loss of water in the PEDOT/PSS film. Using both the DSC and TGA results together provides more refined information about the water content. Indeed, the characteristic energy, E, for dehydration can be estimated from:[35]

$$E = M \frac{\Delta Q}{\Delta W} \qquad (2)$$

where M is the molecular weight of water (18 g mol^{-1}) and ΔQ and ΔW are the amount of heat evolved during the dehydration and the weight loss of water between 21 and 200 °C, respec-tively. ΔQ is estimated from DSC to be −545 J g^{-1}, while the weight loss of PEDOT/PSS is estimated from TGA to be 22.8 wt%, leading to a characteristic energy, E, of around 10.28 kcal mol^{-1}. This energy level is comparable to the energy of moderate hydrogen bonds (4 to 15 kcal mol^{-1}).[36] With this information, we propose a configuration in which the water molecules are hydrogen-bonded with PSS chains, as shown in Fig. 5(c).

Typically, every three or four thiophene unit on PEDOT chains carries a positive charge. The benzene rings in PSS chains carry two kinds of sulfonic groups that can be either ionized SO_3^- or neutral SO_3H. The ionic bonding between SO_3^- and thiophene rings results in a complex structure of PEDOT with PSS.[34] The hydration will start with the fixation of H_2O molecules on the free and highly hygroscopic SO_3H groups.[19] In the molecular structure of PEDOT/PSS shown in Fig. 5(c), we assume that $(C_6H_6O_2S)_m(C_8H_8O_3S)_n$ is the molecular formula of PEDOT/PSS. Based on the weight ratio of PEDOT to PSS (1 : 2.5) and their monomer molecular weights (140 and 182, respec-tively), the m/n ratio is estimated to be 0.443. By taking into consideration that 20 wt% of water was absorbed by the PEDOT/PSS, we write the molecular formula of the "wet" PEDOT/PSS at 65% RH as $(C_6H_6O_2S)_{0.443n} (C_8H_8O_3S)_n (H_2O)_{3.6n}$. This simple formula indicates that three or four water molecules are absorbed by each PSS chain at room temperature, as illustrated in Fig. 5(c). As a result, the microstructure will be dominated by regime 1 as shown in Fig. 4 at room temperature. The films are basically swelled by the water vapor and the weakened hydrogen bonds react with water via the following equation.[32,37]

$$H_2O + PSS(HSO_3) \rightarrow H_3O^+PSS(SO_3)^- \qquad (3)$$

This journal is © The Royal Society of Chemistry 2014

J. Mater. Chem. C, 2014, xx, 1–8 | 5

Thus, the grains easily slide by each other upon mechanical loading at RT as they are weakly connected. By cooling down the film from room temperature to the low temperature state, the water absorbed on the PEDOT/PSS film will form ice crystals, as indicated by the EELS analysis (Fig. 2). It is known that at temperatures near the melting point of ice, the Young's modulus of single ice crystals varies from 8.6 to 12 GPa.[38] This value could go even higher as the temperature reduces. In the low temperature state model, the ice crystals not only restrict the sliding of PSS chains but also contribute to the overall modulus. Moving on to the high temperature state of the PEDOT/PSS film, the hydrogen bonds are strengthened due to the removal of water molecules from the films. There will not be hydrogen bonding between water molecules and PSS chains. The strong co-adhesion between PSS chains comes from the hydrogen bonding between intermolecular or intramolecular PSS chains, as displayed in regime 2 in Fig. 4.

From the above-mentioned results and our microscopical model, it is important to note that a PEDOT/PSS thin film in a normal environment (40–70% RH) is highly loaded with water. This should be considered as the normal configuration of the material in most applications. As a result, it is very important to determine the effect of water on the mechanical and electrical properties of PEDOT/PSS films.

Effect of water on the dynamic mechanical behavior of PEDOT/PSS films

The mechanical strength of PEDOT/PSS comes from the PEDOT nanocrystals and the hydrogen bonds between intermolecular or intramolecular PSS chains. As there is no noticeable change in the d-spacings of crystal planes when measured at LT, RT and HT for PEDOT/PSS films (insets of Fig. 1(a), (c) and (e)), we can eliminate the temperature effect on the modification of the mechanical behavior of PEDOT chains. As mentioned previously, the water absorbed by PSS chains will play an important role in determining the final mechanical behaviors. Therefore, scanning the mechanical behavior by DMA over a wide range of temperatures is a way to track the effect of progressive water on the effective properties.

Fig. 6(a) displays the DMA scan sequences of the PEDOT/PSS film. Fig. 6(b) shows that the storage modulus of the PEDOT/PSS film largely varies during the first scan from −150 to 250 °C. In detail, the modulus of the film reduced from 7.5 GPa at −150 °C to 1.0 GPa at 75 °C in the first scan. Then, the modulus increased again to relatively high values (2.8 GPa at 100 °C and 3.2 GPa at 150 °C). It is necessary to point out that PEDOT/PSS films were annealed in air at 120 °C for two hours before the first DMA scan. However, due to the hygroscopic nature of PEDOT/PSS and high RH (65%), the film readily absorbed up to 20 wt% of water from the environment before we put the sample into the DMA chamber (Fig. S3, ESI†). This result clearly indicates that in the temperature range of 0 to 75 °C, the PEDOT/PSS film contains a large amount of water dissolving from solid into liquid, which turned the film into a rubbery state. The transformation of water from solid to liquid form eases the relative motion of the PEDOT/PSS chains such that the storage modulus
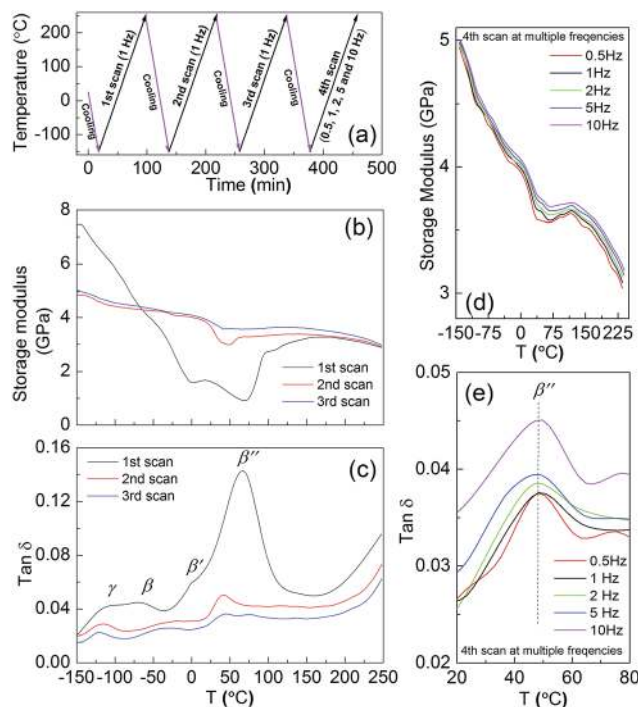

Fig. 6 Dynamic mechanical behavior of the PEDOT/PSS film. (a) Scan sequences of DMA. (b), (c) and (d) Storage modulus, strain and damping factor of the PEDOT/PSS film over the first three scans, respectively (e) and (f) storage modulus and damping factor of the PEDOT/PSS film at multiple frequencies (0.5, 1, 2, 5 and 10 Hz) in the fourth scan, respectively.

is reduced to 1 GPa at 75 °C in the first scan. On the other hand, the film starts to release water quickly after 75 °C, improving its storage modulus and resulting in a contraction of the PEDOT/PSS film between 75 and 100 °C. After 100 °C, there are no dramatic changes in the storage modulus of the PEDOT/PSS film, as most of the PEDOT/PSS grains are connected with each other at 150 °C compared with 100 °C (Fig. 1(f) andS5†). Due to the annealing of the first scan from 100 to 250 °C, the water was almost removed from the PEDOT/PSS. The effect of water on the modulus change of the second and third scans is not obvious anymore.

Fig. 6(c) depicts essentially all changes in the molecular motion of PEDOT/PSS films in three scans at different temperatures. The γ relaxation exhibited in all three scans indicates that the side groups of PSS chains, HSO_3, experience amorphous phase relaxation. The β relaxation at −65 °C is associated with water–HSO_3 interactions. In fact, previous research has shown that the β relaxation of another conjugated polymer, polypyrrole, at −60 °C is also due to the motion of water molecules absorbed in the polymer.[39] Due to the annealing of the PEDOT/PSS film at high temperature (100 to 250 °C), this transition disappears during the second and third scans. The PEDOT chains are in a conjugated form, which causes the chains not to move as easily as amorphous PSS chains. The torsional motion of the aromatic rings in PSS chains dominates the β′ transition. This β′ transition shifts to low temperatures due to the removal of water. Finally, the broad β″ peak in the

first scan shrinks into small peaks during the second and third scans. The reduction of the damping factor indicates that PEDOT/PSS films become more elastic due to the annealing process. In order to determine if this peak is the glass transition, multiple frequency scans (0.5, 1, 2, 5 and 10 Hz) of the PEDOT/PSS film were carried out in the fourth scan of the same sample. Fig. 6(d) indicates that the storage modulus is quite independent of the frequency change. Moreover, there is no obvious tan δ peak shift when the frequency is changed from 0.5 to 10 Hz (Fig. 6(e)). This result indicates that the transition around 49 °C is a first-order reaction like a phase change or some other physical process.[29] As a result, we can remark that the drying of water from PEDOT/PSS films causes this frequency-independent loss process.

Effect of temperature on the electrical conductivity of PEDOT/PSS films

To understand the temperature effects on the electrical transport properties, we measured the temperature dependence in the −150–250 °C range. The conductivity of the PEDOT/PSS film was 0.25 S cm^{-1} (R (21 °C) = 1310 Ω) at RT in air. After the film stabilized in an N_2 atmosphere for 30 min at RT, its conductivity slightly increased to 0.32 S cm^{-1} (R(21 °C) = 1028 Ω). As noted the PEDOT/PSS film contains 22.8 wt% of water (Fig. 5(b)). Given the fact that water has conductivity in the range of 5×10^{-5} to 5×10^{-4} S cm^{-1}, the conductivity increase in the PEDOT/PSS film in an N_2 atmosphere is due to partial water removal from the PEDOT/PSS film. Fig. 7 shows the dependence of temperature on conductivity in PEDOT/PSS films that follow different cooling and heating sequences. The temperature programs generally follow the DMA scanning sequences in Fig. 6(a) without the fourth heating. The film was first cooled from RT (21 °C) to −150 °C and the conductivity of the film was reduced from 0.32 to 0.065 S cm^{-1} (R(−150 °C) = 5000 Ω). The three heating sequences shown in Fig. 7(b) indicate that PEDOT/PSS films exhibit a typical semiconductor behavior with a positive temperature coefficient. Thus, the charge transport regime in PEDOT/PSS films is thermally activated. The conductivity (1.8 and 1.7 S cm^{-1}) during the second and third heating of the film is about six times higher than that of the first heating (0.32 S cm^{-1}) at RT. While the final conductivities are quite close at 250 °C (3.1 S cm^{-1} for the first, 2.92 S cm^{-1} for second and 2.87 S cm^{-1} for third heating). It is worth noting that during the first heating, there was a rapid conductivity increase from 21 to 120 °C compared with second and third heating. This change could be attributed to the water removal process from 16 to 120 °C, as indicated by the investigation of the thermal properties on the film (Fig. 5 and 6). During the cooling process, the good consistency of the third and fourth cooling curves indicates that water had no effect on the conductivity of the PEDOT/PSS film after the heating process (Fig. 7(a)).

With regard to the electrical conductivity of PEDOT/PSS at different temperatures, the above-mentioned model (Fig. 4) also provides structure and electrical property correlations. In the core–shell structure of PEDOT/PSS, the insulating shell-rich PSS boundaries contribute significantly to the overall resistivity of the film.[34] At room temperature, swelled PEDOT/PSS with residual water on PSS boundaries will reduce the overall conductivity of the film. Removal of the water by heating or putting the film in a non-reactive gas like N_2 will reduce the boundary size. We note that the highest conductivities are achieved at high temperatures. Not only is the total number of particle boundaries reduced, but the effective "size" of the particle boundaries is also reduced. At low temperatures, some of the localized electrons do not have sufficient thermal energy to overcome barriers that are caused by potential wells of variable depth and hopping to a neighboring site. Thus, the conduction process in low temperatures involves overcoming the barriers between the localized electrons[40] and the PSS boundaries.

4 Conclusions

We have demonstrated that the microstructure of PEDOT/PSS films depends on the water content in a broad range of temperatures. HAADF-STEM combined with EELS and AFM analyses provided the evidence of microstructural changes in PEDOT/PSS films at different temperatures and allowed us to formulate a microscopic model. At room temperature, the water molecules weaken the adhesion between PEDOT/PSS grains, which results in a low modulus. At low temperature, the water becomes ice crystals that act as reinforcements to enhance the modulus of PEDOT/PSS. Finally, at high temperatures, the water molecules are totally removed and the interaction among PEDOT/PSS grains is dominated by enhanced hydrogen bonding of PSS chains. Understanding the role of water in determining the mechanical behavior of these films is critical for fabricating devices containing PEDOT/PSS layers and guiding the development of flexible electronic devices. This study highlights the importance of considering microstructure changes as a design element in integrating conductive polymers into flexible devices.
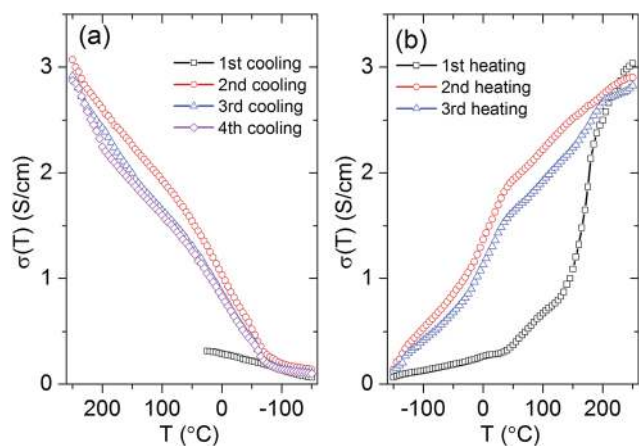

Fig. 7 The dependence of temperature on conductivity of the PEDOT/PSS film. (a) During the four cooling stages at a cooling rate of 10 K min^{-1}. (b) During the three heating stages at a heating rate of 5 K min^{-1}.

This journal is © The Royal Society of Chemistry 2014

J. Mater. Chem. C, 2014, xx, 1–8 | 7

Acknowledgements

References

1 R. Noriega, J. Rivnay, K. Vandewal, F. Koch, N. Stingelin, P. Smith, M. Toney and A. Salleo, *Nat. Mater.*, 2013, **12**, 1038.

2 G. Kim, L. Shao, K. Zhang and K. Pipe, *Nat. Mater.*, 2013, **12**, 719.

3 B. Kim, E. Jeong, J. Chung, S. Seo, B. Koo and J. Kim, *Nat. Mater.*, 2013, **12**, 659–664.

4 D. A. Mengistie, P. C. Wang and C. W. Chu, *J. Mater. Chem. A*, 2013, **1**, 9907.

5 J.-C. Lin, W.-Y. Lee, H.-C. Wu, C.-C. Chou, Y.-C. Chiu, Y.-S. Sun and W.-C. Chen, *J. Mater. Chem.*, 2012, **22**, 14682.

6 H.-Y. Chen, H.-P. Shen, C.-H. Wu, W.-Y. Chiu, W.-C. Chen and H.-J. Tai, *J. Mater. Chem. C*, 2013, **1**, 5351.

7 D. Alemu, H. Wei, K. Ho and C. Chu, *Energy Environ. Sci.*, 2012, **5**, 9662.

8 J. T. Kim, J. Pyo, J. Rho, J. H. Ahn, J. H. Je and G. Margaritondo, *ACS Macro Lett.*, 2012, **1**, 375.

9 K. Chou, B. Yan, R. Li, E. Li, K. Zhao, D. Anjum, S. Alvarez, R. Gassaway, A. Biocca, S. Thoroddsen, A. Hexemer and A. Amassian, *Adv. Mater.*, 2013, **25**, 1923.

10 H. Miura, Y. Fukuyama, T. Sunda, B. Lin, J. Zhou, J. Takizawa, A. Ohmori and M. Kimura, *Adv. Eng. Mater.*, 2014, **16**, 550.

11 J. Ouyang, Q. Xu, C. Chu, Y. Yang, G. Li and J. Shinar, *Polymer*, 2004, **45**, 8443.

12 J. Ouyang, C. Chu, F. Chen, Q. Xi and Y. Yang, *Adv. Funct. Mater.*, 2005, **15**, 203.

13 B. H. Fan, X. G. Mei and J. Y. Ouyang, *Macromolecules*, 2008, **41**, 5971.

14 Y. Xia and J. Ouyang, *Org. Electron.*, 2010, **11**, 1129.

15 K. Sun, Y. Xia and J. Ouyang, *Sol. Energy Mater. Sol. Cells*, 2012, **97**, 89.

16 Y. Xia, K. Sun and J. Ouyang, *Adv. Mater.*, 2012, **24**, 2436.

17 J. E. McCarthy, C. A. Hanley, L. J. Brennan, V. G. Lambertini and Y. K. Gun'ko, *J. Mater. Chem. C*, 2014, **2**, 764.

18 N. Kim, S. Kee, B. Lee, Y. Kahng, Y. Jo, B. Kim and K. Lee, *Adv. Mater.*, 2014, **26**, 2268.

19 H. Okuzaki, H. Suzuki and T. Ito, *J. Phys. Chem. B*, 2009, **113**, 11378.

20 U. Lang, N. Naujoks and J. Dual, *Synth. Met.*, 2009, **159**, 473.

21 J. Zhou, T. Fukawa, H. Shirai and M. Kimura, *Macromol. Mater. Eng.*, 2010, **295**, 671.

22 J. Zhou, Q. Gao, T. Fukawa, H. Shirai and M. Kimura, *Nanotechnology*, 2011, **22**.

23 J. Zhou, T. Fukawa and M. Kimura, *Polym. J.*, 2011, **43**, 849.

24 J. Zhou and G. Lubineau, *ACS Appl. Mater. Interfaces*, 2013, **5**, 6189.

25 U. Lang, E. Müller, N. Naujoks and J. Dual, *Adv. Funct. Mater.*, 2009, **19**, 1215.

26 J. Zhou, I. Ventura and G. Lubineau, *Ind. Eng. Chem. Res.*, 2014, **53**, 3539.

27 D. Williams and C. Carter, Springer, Boca Raton, London and New York, 2nd edn, 2009, pp. 79–100.

28 J. Duncan, in *Principles and Applications of Mechanical Thermal Analysis*, ed. P. Gabbott, Blackwell, New Delhi, 1st edn, 2008, pp. 129–131.

29 J. Duncan, in *Principles and Applications of Mechanical Thermal Analysis*, ed. P. Gabbott, Blackwell, New Delhi, 1st edn, 2008, pp. 139–149.

30 R. Pytel, E. Thomas and I. Hunter, *Chem. Mater.*, 2006, **18**, 861.

31 R. Pytel, E. Thomas, Y. Chen and I. Hunter, *Polymer*, 2008, **49**, 1338.

32 S. Dupont, F. Novoa, E. Voroshazi and R. Dauskardt, *Adv. Funct. Mater.*, 2014, **24**, 1325.

33 T. Takano, H. Masunaga, A. Fujiwara, H. Okuzaki and T. Sasaki, *Macromolecules*, 2012, **45**, 3859.

34 S. Kirchmeyer, K. Reuter and J. Simpson, in *Poly(3,4-Ethylene- Dioxythiophene) Scientific Importance, Remarkable Properties, and Applications*, ed. T. Skotheim and J. Reynolds, CRC press, Boca Raton, London and New York, 3rd edn, 2007, vol. 1, pp. 79–100.

35 E. Matveeva, R. Calleja and V. Parkhutik, *Synth. Met.*, 1995, **72**, 105.

36 M. Saggu, N. Levinson and S. Boxer, *J. Am. Chem. Soc.*, 2012, **134**, 18986.

37 M. De Jong, L. Van IJzendoorn and M. de Voigt, *Appl. Phys. Lett.*, 2000, **77**, 2255.

38 E. Schulson, *JOM*, 1999, **51**, 21.

39 D. Lesueur and N. Alberola, *Synth. Met.*, 1997, **88**, 133.

40 R. Hummel, Springer, New York, Dordrecht, Heidelberg and London, 4th edn, 2010, pp. 122–126.

8 | *J. Mater. Chem. C*, 2014, **xx**, 1–8

This journal is © The Royal Society of Chemistry 2014